Numerical Investigation of Cross-Flow Around a Circular Cylinder at a Low-Reynolds Number Flow Under an Electromagnetic Force

Seong-Jae Kim*

Researcher, LG Electronics, Digital Appliance Research Laboratory, 327-23, Gasan-Dong, Geumchun-Gu, Seoul 152-020, Korea

Choung Mook Lee

Professor, Department of Mechanical Engineering and Advanced Fluids Engineering Research Center, Pohang University of Science and Technology, San-31, Hyoja-Dong, Pohang, Kyungbuk 790-784, Korea

The effect of the electromagnetic force (or Lorentz force) on the flow behavior around a circular cylinder is investigated by computation. Two-dimensional unsteady flow computation for $Re=10^2$ is carried out using a numerical method of finite difference approximation in a curvilinear body-fitted coordinate system by solving the momentum equations including the Lorentz force as a body force. The effect of spatial variations of the Lorentz forcing region and forcing direction along the cylinder circumference is investigated. The numerical results show that the Lorentz force can effectively suppress the flow separation and oscillation of the lift force of circular cylinder cross-flow, leading to reduction of drag.

Key Words : MHD Flow, Separation Control, Drag Reduction, Lift Suppression, Circular -Cylinder Flow

Nomenclature

B_k : Magnetic flux density vector (tesla)
D : Cylinder diameter
E_j : Electric field intensity vector (volt/m)
f_n : Vortex shedding frequency
J_j : Electric current density vector (ampere/area)
N : Interaction parameter $(=J_oB_oD/(\rho U_o^2))$
Re : Reynolds number $(=U_oD/\nu)$
S_n : Strouhal number $(=f_nD/U_o)$
$\tilde{t}$: Non-dimensional time $(=U_ot/D)$
U_o : Upstream flow velocity
ρ : Fluid density
σ : Electric conductivity (mho/m)
ν : Kinematic viscosity

* Corresponding Author,
  E-mail : kimsj@lge.com
  TEL : +82-54-279-2834; **FAX :** +82-54-279-3199
  Researcher, LG Electronics, Digital Appliance Research Laboratory, 327-23, Gasan-Dong, Geumchun-Gu, Seoul 152-020, Korea. (Manuscript **Received** May 15, 2001; **Revised** December 13, 2001)

1. Introduction

MHD (Magnetohydrodynamics) flow has been a subject investigated by many researchers since Ritchie succeeded in pumping water using the Lorentz force in 1832. Recently, along with the attempts to explore MHD propulsion (Kim and Lee, 1997) and MHD power generation, efforts to control the fluid flow using the electromagnetic force (or the Lorentz force) have been made by many investigators. Henoch and Meng (1991) and Nosenchuck and Brown (1993) used the Lorentz force to retard the transition to the turbulent boundary layer and reduce frictional drag force. In the recent International Symposium on Seawater Drag Reduction in Rhode Island, USA, a number of works using the Lorentz force to reduce the drag in turbulent flows were reported
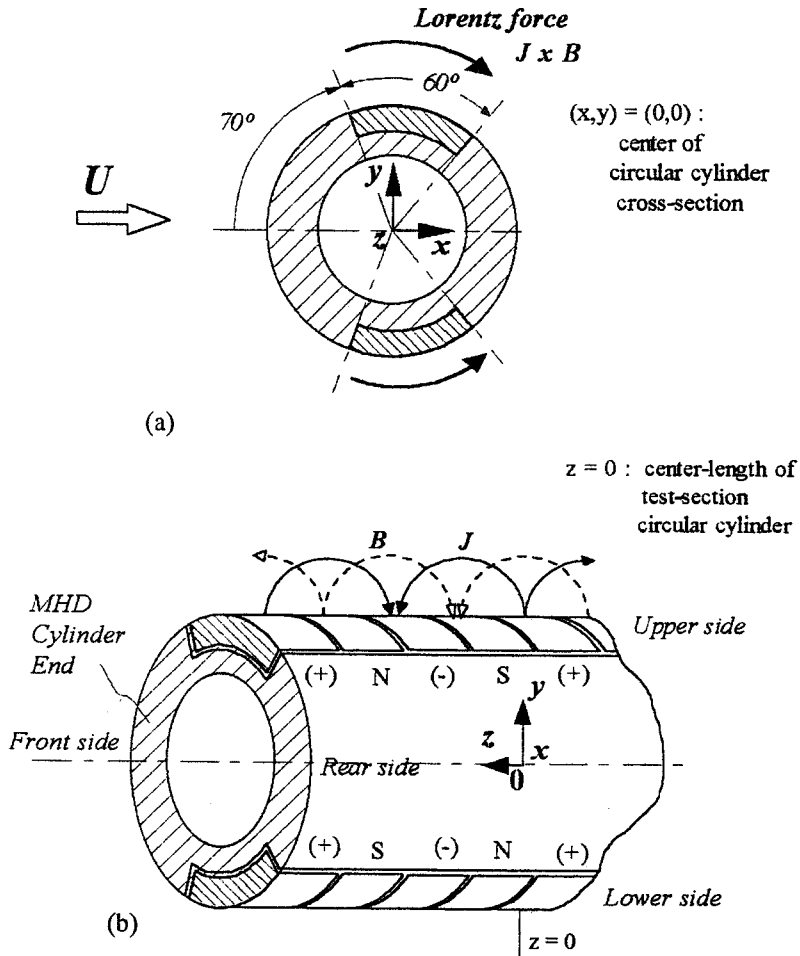
Fig. 1 Circular cylinder for electromagnetic flow control(Kim & Lee, 2000):(a) Cross-sectional view; (b) Installation of electrodes and magnets

(see Meng, 1998) along with other conventional flow control methods.

Kim and Lee(2000) conducted an experiment using a circular cylinder where the electrodes and magnets were installed in an alternate sequence in the axial direction of the cylinder to generate the Lorentz force in the circumferential direction. They installed the electrodes and magnets in the region of 70° ~ 130° along the cylinder circumference where the flow separation mainly occurred. They found that the Lorentz force applied parallel to the flow direction reduced the drag force significantly, especially at low-Reynolds number flows. In the paper, the visualization of the suppression of flow separation and the reduc-

tion of a width of the wake region behind the circular cylinder were clearly demonstrated. Kim and Lee(2001) also confirmed experimentally that the Lorentz force could effectively suppress an oscillatory lift force acting on a circular cylinder by applying both continuous and time-pulsating Lorentz forces. Figure 1 shows the schematic description of the circular cylinder used by Kim and Lee(2000).

In the present work, a computational investigation is carried out to study the effect of variation of the Lorentz forcing region and the forcing direction at $Re = 10^2$ on the flow, drag and lift of the circular cylinder used in the experimental investigation of Kim and Lee(2000). Four types

Table 1 Comparison with the previous computations for $Re = 10^2$ without Lorentz force

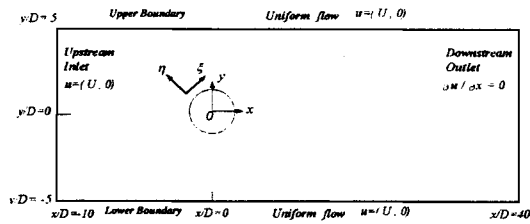| Case	Time-step (non-dim.)	Onset of Oscillation (t)	Strouhal number	C_L amplitude	Averaged C_L
Present* Computation	0.02	44.4 (approx.)	0.161	0.26	1.165
Karniadakis (1989)	0.018	72	0.179		
Braza (1990)	0.02	60	0.165	0.37	1.253
Engelman (1990)	0.026–0.033		0.161–0.172	0.35	1.4–1.42
Roshko's (1954)			0.167		
Williamson's (1988)			0.164		

* The lateral boundary is limited to $y/D = \pm 5$

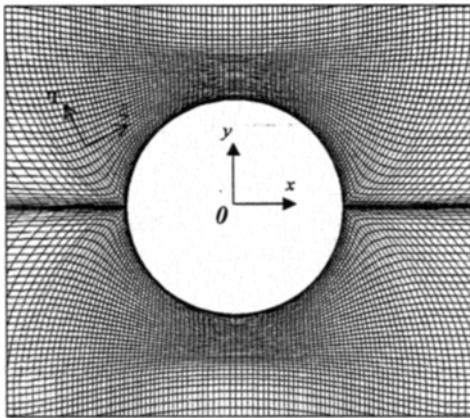**Fig. 2** Domain for flow computation and its coordinate system

Fig. 3 Extended view of the grid system used in the present computation

Fig. 4 Computed histories of the lift (a) and drag (b) coefficients for $Re = 10^2$ without Lorentz force

of the Lorentz forcing are chosen in the computation: circumferential Lorentz forcings parallel and opposite to the flow and normal Lorentz forcings inward to and outward from th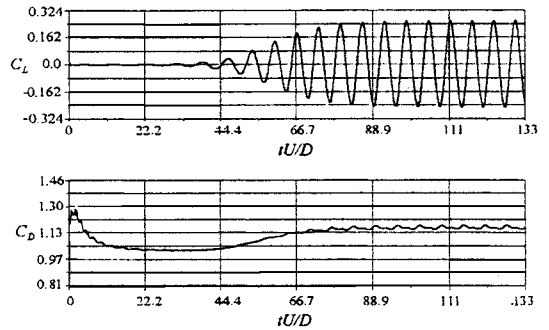e cylinder circumference. Each type of the Lorentz force is applied in three regions along the cylinder circumference: $20° \sim 80°$, $70° \sim 130°$, and $120° \sim 180°$ from the fore stagnation point for both upper and lower sides of the cylinder.

2. Governing Equations

The Lorentz force is generated in a conducting fluid by the vector product of the current density vector, J_j (ampere/area), and the magnetic flux density, B_k (tesla), as $\varepsilon_{ijk} J_j B_k$ where the subscript implies the component of the coordinates (x, y, z) and ε_{ijk} is the alternating permutation tensor. The electric current density vector is described by the Ohm's law of $J_j = \sigma (E_j + \varepsilon_{jlm} u_l B_m)$ where σ is the electric conduc-

Case-P1   Case-P2   Case-P3

Case-O1   Case-O2   Case-O3

Case-I1   Case-I2   Case-I3

Case-N1   Case-N2   Case-N3
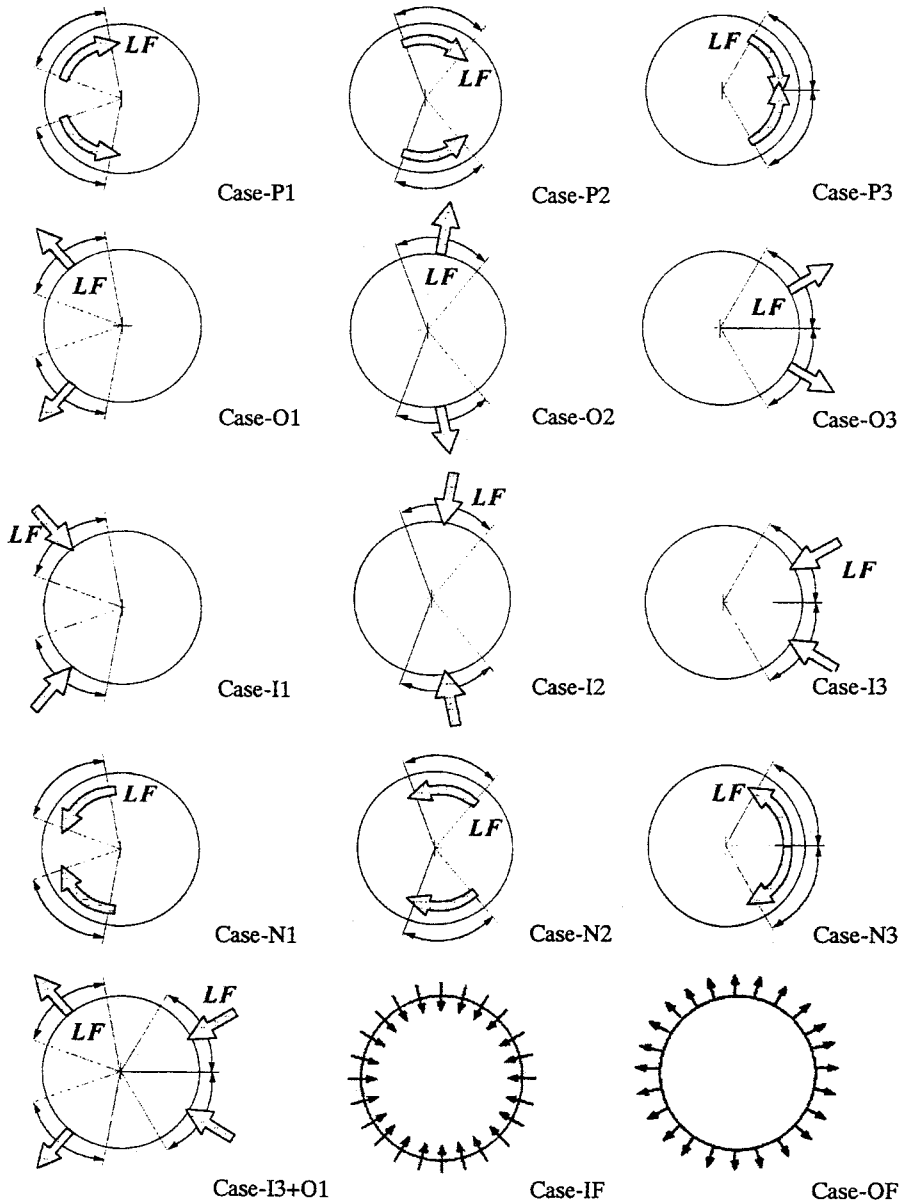
Case-I3+O1   Case-IF   Case-OF

Fig. 5 Types of the Lorentz force in the computation

tivity and E_j is the electric field vector (volt/m). When the electric current induced by the magnetic field is small, i.e., $\varepsilon_{jlm}u_l B_m = 0$, the current density becomes simply $J_j = \sigma E_j$, where $u_l = (u, v)$ is the fluid velocity vector. The non-dimensional form of the momentum equations including the Lorentz force as a body force can be expressed, by using $u_j = u_j^*/U_o$, $t = U_o t^*/D$ $\sigma E_j = \sigma^* E_j^*/J_o$ and

$B_j = B_j^*/B_o$ where the asterisk denotes the dimensional quantity, as

$$\frac{\partial u_i}{\partial t} + u_j \frac{\partial u_i}{\partial x_j} = -\frac{\partial p}{\partial x_i} + \frac{1}{Re}\frac{\partial^2 u_i}{\partial x_j^2} + N(\sigma \varepsilon_{ijk}E_j B_k) \quad (1)$$

where p is the pressure, $Re = U_o D/\nu$ (Reynolds number), ν the kinematic viscosity, D the cylinder diameter, $N = J_o B_o D/(\rho U_o^2)$ (Interaction parameter), B_o the characteristic magnetic

Table 2   Computed time-averaged drag and lift coefficients under the various Lorentz forces at $Re=10^2$

LF mode	LF region	Case	C_{Dp}	C_{Df}	C_D	C_L Amp.	Strouhal number S_n
No LF	–		0.86	0.31	1.16	0.26	0.16
Positive LF	20–80	P1	0.58	0.92	1.50	0.13	0.23
	70–130	P2	0.15	1.06	1.21	0	0
	120–180	P3	0.36	0.70	1.05	0	0
Outward LF	20–80	O1	0.31	0.25	0.56	0.4	0.14
	70–130	O2	1.29	0.36	1.64	0.60	0.16
	120–180	O3	1.67	0.40	2.07	0.44	0.16
Inward LF	20–80	I1	1.45	0.37	1.82	0.18	0.17
	70–130	I2	0.51	0.27	0.78	0.05	0.15
	120–180	I3	0.11	0.24	0.34	0.63	0.15
Negative LF	20–80	N1	0.95	−0.42	0.53	0.63	0.14
	70–130	N2	3.12	−0.27	2.86	2.36	0.13
	120–180	N3	2.39	0.12	2.52	2.27	0.14
Inward(120–180) & Outward(20–80)		I3+O1	0.02	0.23	0.25	0.58	0.15
Inward-normal (0~360)		IF	0.79	0.32	1.11	0.27	0.16
Outward-normal (0~360)		OF	0.92	0.32	1.24	0.25	0.16

strength, J_o the characteristic electric strength, and U_o the undisturbed upstream velocity. In the present investigation, the important physical parameters are the Reynolds number (Re), the Strouhal number $(S_n=f_nD/U_o$ where f_n is the vortex shedding frequency), and the interaction parameter (N) which implies the ratio of the applied electromagnetic force to the fluid inertia force.

3. Numerical Analysis

A time-dependent two-dimensional incompressible flow around a circular cylinder is directly calculated at $Re=10^2$ by solving the Navier-Stokes equations including the Lorentz force as a body force. The finite difference approximations are used to discretize the continuity and momentum equations transformed to a body-fitted coordinate system (ξ, η). A second-order central differencing method is adopted for the diffusion and source terms. The convective term in the momentum equation is approximated employing the third-order accurate QUICK (quadratic upstream interpolation for convective kinetics) scheme following Hayase et al. (1990) which is known to be stable and fast-converging. An unsteady SIMPLE-C (semi-implicit pressure linked equation-consistent) velocity-pressure correction algorithm with a staggered grid system is employed for the curvilinear Navier-Stokes equations.

Figure 2 shows the computational domain where the origin of the coordinate $(x=0, y=0)$ is located at the center of the circular cylinder. Fluid flows in the positive x-direction and the y-axis is normal to the flow direction. The boundary condition of the undisturbed uniform flow of $u_j=(U_o, 0)$ is imposed at the upstream, the upper and lower boundaries. The Neumann outflow condition is imposed at the downstream, i.e. $\partial u_j/\partial x=0$ which was used by Karniadakis(1989) with
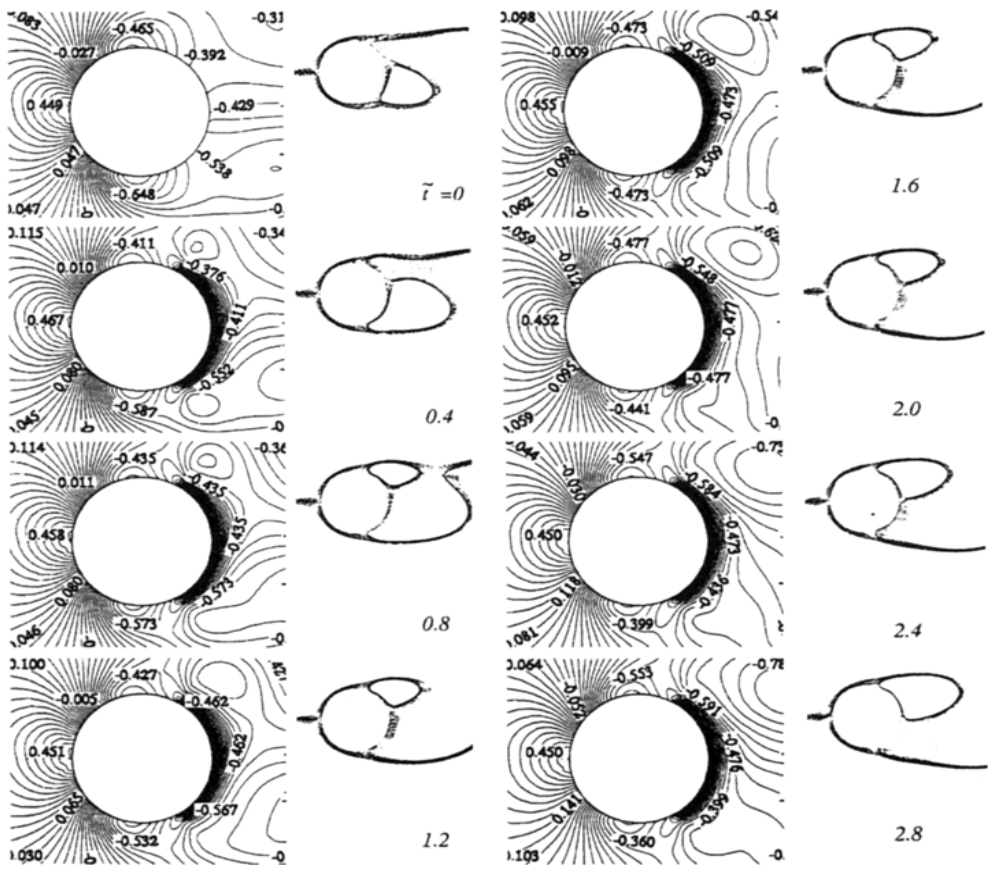
Fig. 6 Computed instantaneous pressure contours and corresponding streamline patterns at $N=20$ and $Re=10^2$ for the case of Inward-normal LF at $\theta=120°\sim180°$

reasonable results. The upstream and downstream boundaries are located at $x/D=-10$ and 40, respectively, and the upper and lower boundaries are located at $y/D=5$ and -5, respectively.

Figure 3 shows the grid distribution around the circular cylinder used in the computation. The grid system is of a H-type rectangular domain where the Cartesian coordinates of (x, y) are transformed to the generalized body fitted coordinates of (ξ, η). The total numbers of the nodes of the grid in ξ and η directions are 190 and 94, respectively, and the number of the grid nodes in the ξ-direction distributed on the half-cylinder surface is 67. The grid system was generated by solving an elliptic-type partial differential equation.

The cross-flow around a circular cylinder at $Re=10^2$ belongs to the pure Karman vortex

range where the regular Karman vortex street is formed and the Strouhal number S_n is found experimentally to be $0.16\sim0.17$(Norberg, 1994). The computational results of the drag force coefficient and the Strouhal number obtained by previous investigators show that the values range from 1.2 to 1.5 and from 0.16 to 0.18, respectively, as shown in Table 1. In the table, $\tilde{t}$ indicates the non-dimensionalized time defined as $\tilde{t}=Ut/D$. In the present computation, the blockage ratio of $y/D=5$ is 10 % and the drag and lift coefficients and the Strouhal numbers in Table 1 are the values corrected according to the blockage ratio based on a constant mass-flux. The correction equation is $C_D=C_D'(1\text{-A/S})^2$ where C_D', A, and S are the computed drag coefficient, the projected frontal area$(D\times L)$, and the width of the computation domain(W) times the cylinder length
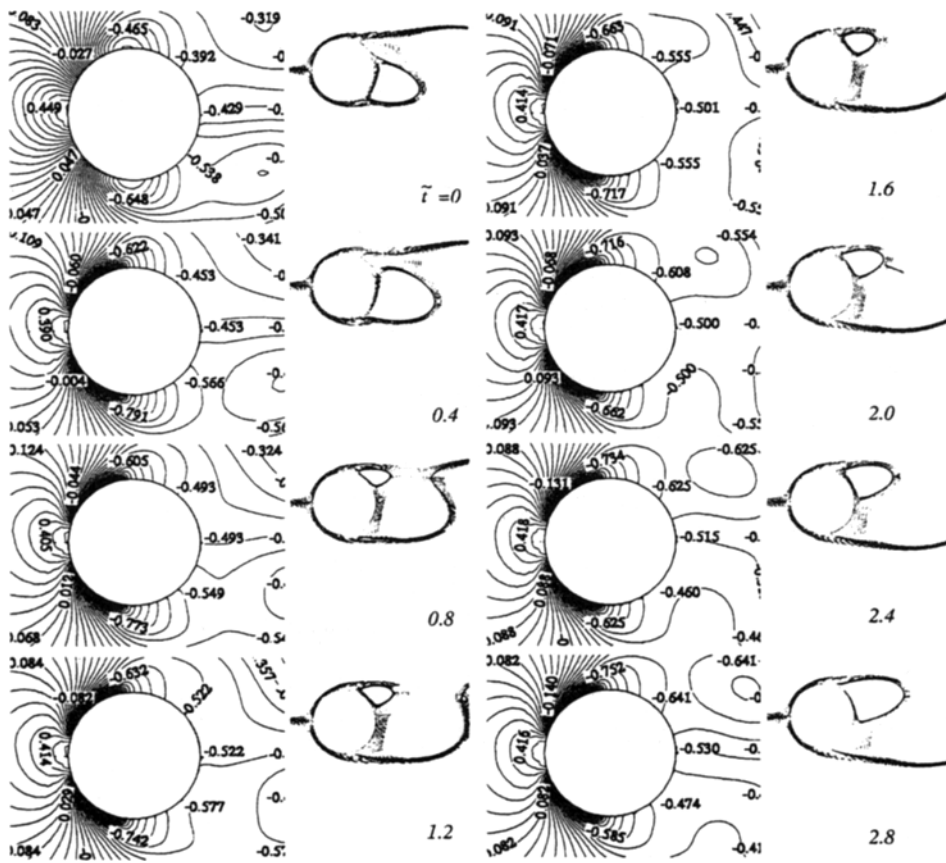
Fig. 7 Computed instantaneous pressure contours and corresponding streamline patterns at $N=20$ and $Re=10^2$ for the case of Outward-normal LF at $\theta=20°\sim80°$

$(W \times L)$, respectively.

Figure 4(a) shows the time history of the lift force coefficient where after a certain time step the lift coefficient begins to oscillate implying that the symmetry of the steady flow separation breaks down. In the stage of the periodic vortex shedding in Fig. 4(a), the lift coefficient oscillates within the amplitude of about 0.26. Literatures suggest that the computed lift coefficient varies with an amplitude in the range of 0.35~0.37(Persillon et al., 1998; Engelman, 1990). Figure 4(b) shows the time history of the drag force coefficient. The phase-averaged drag coefficient(C_D) and the Strouhal number(S_n) in the regularly oscillating region in Fig. 4(b) are found to be 1.17 and 0.16, respectively. The flow begins to oscillate approximately after $\tilde{t}=44.4$ which is somewhat earlier than the result of Karniadakis(1989) in

which the onset of oscillation started at time $\tilde{t}=$ 72. The computation for $y/D=10$ is conducted to check the dependency of the present code on the vertical boundary distance in the case without Lorentz force. The averaged drag coefficient is found to be 1.21 which is slightly larger than the value for $y/D=5$. The Strouhal number for $y/D=10$ is found to be 0.16 which is very close to the value at $y/D=5$. In general, it would be desirable to choose the vertical boundary distance to be $y/D>10$ to avoid the blockage effect. The present computation without Lorentz force shows difference to some extent from those of other researchers except for the values of the Strouhal number. One reason for the difference is due to the narrower computation domain used in the present work. For the purpose of investigating the effect of the local Lorentz forcing on the flow
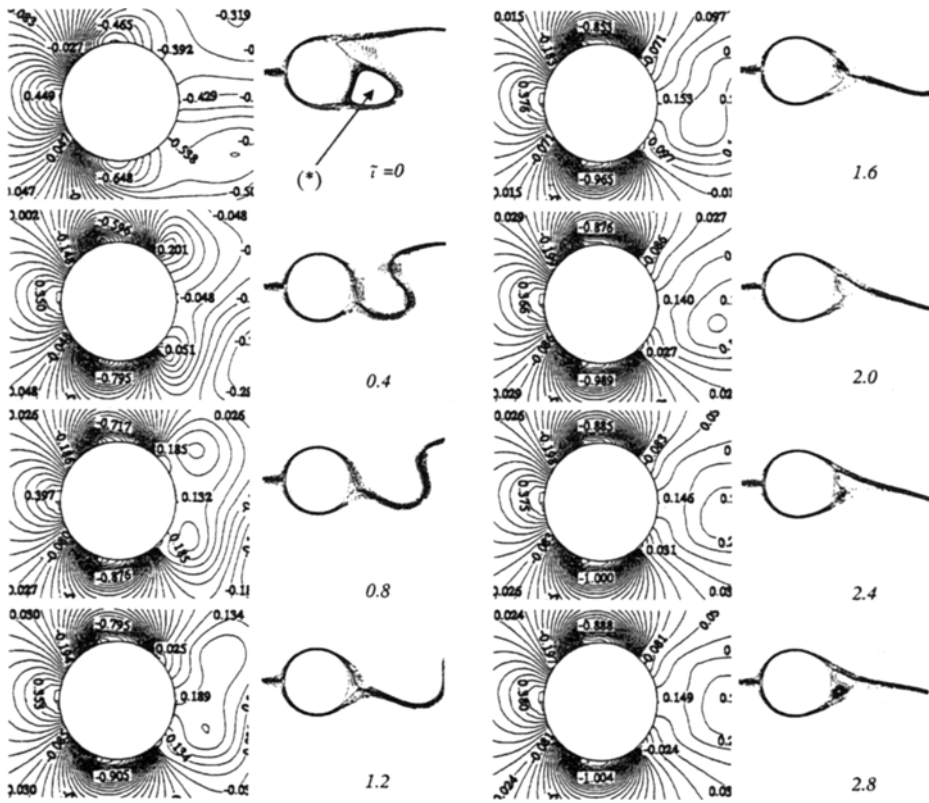
Fig. 8 Computed instantaneous pressure contours and corresponding streamline patterns at $N=20$ and $Re=10^2$ for the case of Positive LF at $\theta=70°\sim130°$

around a circular cylinder, the blockage effect may not be of significant concern, provided the computations are performed under an identical inflow condition for various local Lorentz forcings. Thus, for the sake of quick convergence and the consequent computation-time saving, the boundary size of $y/D=\pm5$ was chosen.

The Lorentz forcing regions along the cylinder circumference are divided into the following three cases: before the flow separation point($\theta=20°\sim80°$ from the fore stagnation point), within the region where the flow normally separates($70°\sim130°$), and after the flow separation point($120°\sim180°$) on both of the upper and lower sides of the circular cylinder. The Lorentz force is applied in the circumferential and radial directions of the circular cylinder. In the circumferential direction, the Lorentz force is applied in the direction of the flow(Positive Lorentz force(LF)) or opposite to the flow(Negative LF) and, in the radial direc-

tion, the Lorentz force is applied inward to(In-ward-normal LF) or outward from the cylinder surface(Outward-normal LF). Figrue 5 shows each type of the 15 forcing cases taken into account in the present computation. The Lorentz force distribution in the radial coordinate(r) of the circular cylinder is regressed in the form of C_1 $exp(-C_2\ r)$ showing an exponential decay where C_1 is the constant linearly proportional to the applied Lorentz force strength and C_2 is the constant related to the width of the electrode and magnet. Both C_1 and C_2 are the functions of width of electrode and magnet. The three -dimensional computation was carried out to obtain the electric and magnetic field potential functions to calculate the Lorentz force distribut-ion. Under the electromagnetic configuration as shown in Fig. 1(b), the Lorentz force is periodically distributed in the axial direction of the circular cylinder. The averaged Lorentz force
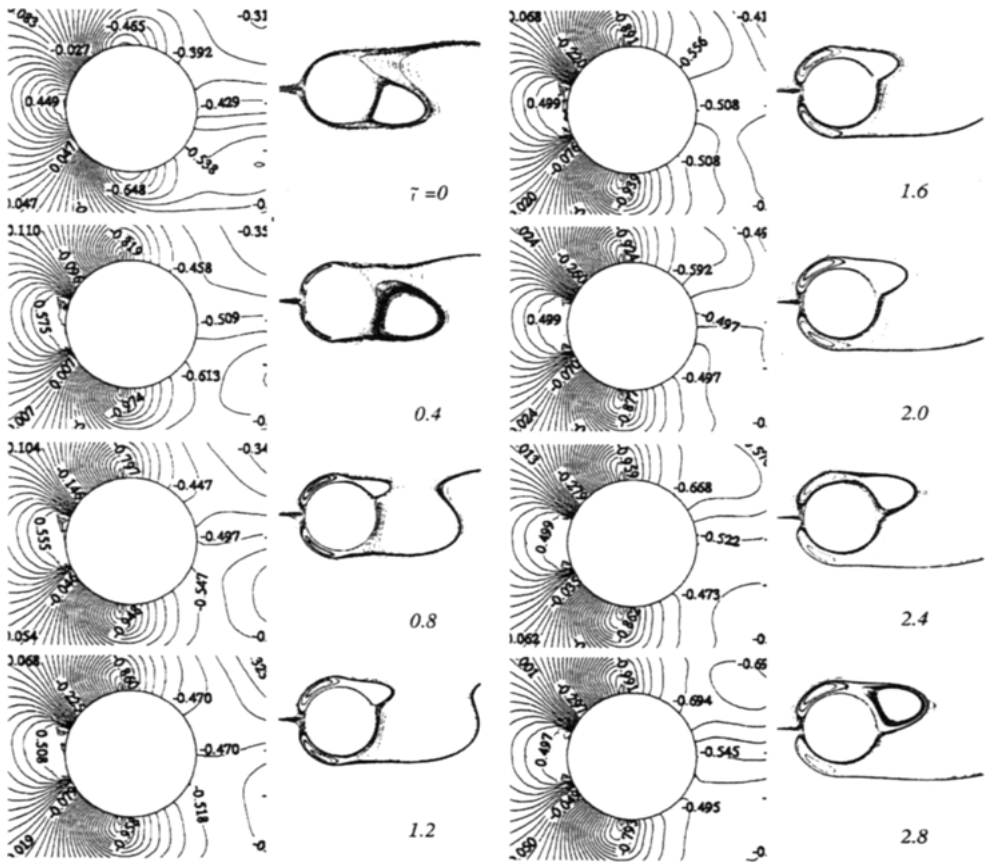
Fig. 9 Computed instantaneous pressure contours and corresponding streamline patterns at $N=20$ and $Re=10^2$ for the case of Negative LF at $\theta=20°\sim80°$

in the axial direction is used in the present two dimensional flow computation. The interaction parameter at the cylinder surface $(r=0)$ is set to be $N=20$. The difficulty encountered was that our experimental capability was limited to $10^3<Re<10^4$, whereas the numerical capability was limited to $Re<200$. Thus, no direct comparisons of the numerical results with the experimental results could be made. However, since the computational reliability at $Re=10^2$ was higher, we performed the computation at this low Reynolds number to investigate the effect of the local Lorentz forcing.

For the Reynolds number range of $O(10^3)$ which is the condition of the previous experiment by Kim and Lee (2000;2001), to obtain the detailed flow structures around the circular cylinder,

the three dimensional computation with a high resolution in space and time should be carried out. However, since it is difficult to calculate the high Reynolds number flow with the present computing capability, the computation is carried out at $Re=10^2$.

4. Results and Discussion

Table 2 shows the computed time-averaged drag force coefficient (C_D), the amplitude of the oscillating lift force $(C_{L\ Amp.})$, and the Strouhal number (S_n) under each type of the Lorentz forces. In the table, C_{Dp} and C_{Df} represent the form and frictional drag force coefficients, respectively. In the following discussion, the simplified notations of P, N, O, and I are used for the
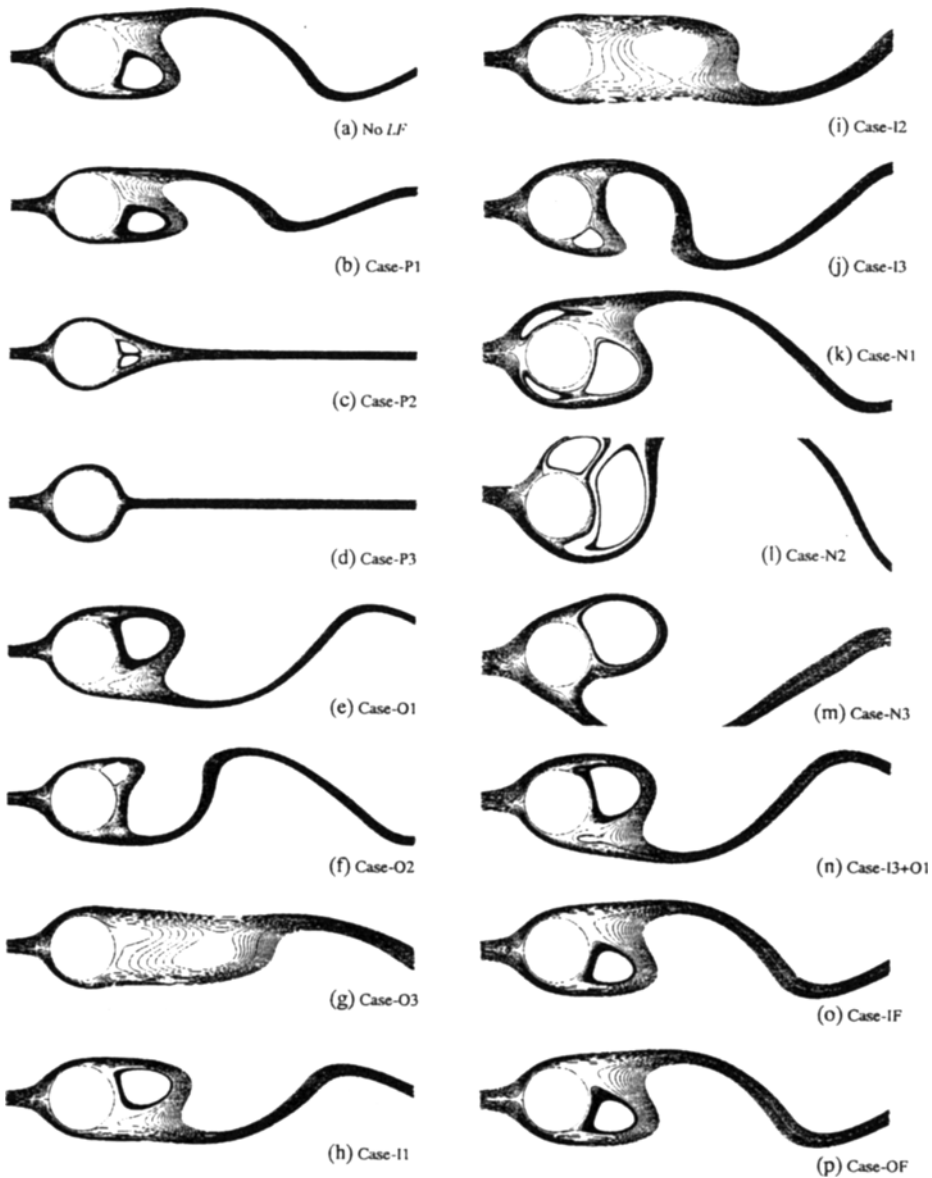
Fig. 10 Computed instantaneous streamlines at $N=20$ and $Re=10^2$

Positive LF, the Negative LF, the Outward-normal LF, and the Inward-normal LF, respectively. The forcing regions of $\theta=20°\sim80°$, $70°\sim130°$, and $120°\sim180°$ are denoted by attaching the number of 1, 2 and 3, respectively, after the types of the forcing directions of P, O, I, and N. It is written as Case-P1, for example, when the Positive LF is applied in the region of $\theta=20°\sim80°$.

The most effective forcing modes for drag re-duction turned out to be the forcing types in the order of Case-I3+O1, Case-I3 and Case-O1. But in the case of Case-I3+O1, the power consump-tion for the drag reduction is twice the magnitude of the other two cases, so that, in respect of the power efficiency, it can be judged that the Case -I3+O1 is not so effective as the other two types of the Lorentz forcing. Despite the drag reduction, there occurs a slight increase in the amplitude of the oscillating lift force under the Lorentz

forcings of Case-I3 and Case-O1. Figures 6 and 7 show the instantaneous pressure contours and the corresponding flow patterns with respect to time under the Lorentz forcings of Case-I3 and Case-O1, respectively. In the figure, $\tilde{t}=0$ indicates the case without Lorentz forcing. With the value of the Strouhal number as 0.16, the period for one vortex shedding process becomes $\tilde{t}=6.25$, but the results are shown only up to $\tilde{t}=2.8$ in the figures to illustrate a part of one-cycle time histories. Although the two forcing types of Case-I3 (Fig. 6) and Case-O1 (Fig. 7) show an obvious difference in the pressure and drag (Table 2), they show similar flow patterns. It is interesting to note that the both cases show the reduction in the drag force in different manners. That is, the forcing of Case-I3 increases the pressure in the rear part of the cylinder while the forcing of Case-O1 decreases the pressure in the front part of the cylinder, thus reducing the drag of the cylinder. In Fig. 6, it is shown that the streamline is displaced to some extent to the outer region of the circular cylinder possibly due to the increase of the surface pressure in the rear part of the cylinder under the Lorentz forcing of Case-I3. Another difference found between the two forcing types is in slight difference in the size of the evolving vortex behind the circular cylinder; otherwise the time-dependent flow patterns are very similar to each other.

Under the Lorentz forcings of Case-P2 and Case-P3, the amplitude of the lift force oscillation is found to be reduced nearly to zero while the total drag force is changed slightly due to the contribution of the increased frictional drag. But when the Reynolds number increases, the portion of the frictional drag force is reduced and the total drag force becomes nearly the same as the form drag. Consequently, the increase in the frictional drag force due to the Positive Lorentz forcing can be neglected compared to the decrease in the form drag. It is expected that the Positive Lorentz forcing can be a useful type for stabilizing the flow and reducing the drag force.

In Fig. 8 the computed instantaneous pressure distribution and the streamline patterns are shown for Case-P2. Due to the Positive Lorentz

forcing the streamlines are maintained to be attached to the cylinder surface to the far rear of the cylinder, thus moving the separation point to the rearside of the cylinder as well. As a result, the large vortex ((*) at $\tilde{t}=0$) in Fig. 8, generated periodically when the Lorentz force is absent, is quickly swept away from the cylinder immediately after the commencement of the Lorentz forcing and thereafter the large vortex no longer reappears. As the time increases after the Lorentz forcing, the flow becomes steady and the pressure distributions at the upper and the lower sides of the cylinder become symmetric. The flow becomes stable and the width of the wake region is also reduced significantly.

Figure 9 shows the instantaneous pressure contours and the corresponding streamline patterns under the Lorentz force of Case-N1. For the case of the Negative Lorentz force, it has been reported by Kim and Lee (2000) that the flow was considerably disturbed and the drag force was drastically increased. In the present computation for $Re=10^2$, as shown in Table 2, although the Lorentz forcings of Case-N2 and Case-N3 reduce the frictional force, the total drag force is greatly increased due to the increased form drag. It is interesting to note in Fig. 9 the large twin vortices generated in the upper and the lower sides of the fore part of the circular cylinder.

The instantaneous streamline patterns for all the 15 types of the Lorentz forces are compared in Fig. 10. The instantaneous time $\tilde{t}$ chosen for each case in Fig. 10 is the instant at which the streamline under the Lorentz forcing of Case-P3 becomes attached up to rear stagnation point to form a symmetrical flow pattern as in the potential flow. Under the Lorentz forcing of Case-P1, there appears no noticeable reduction in the width of the wake region. On the other hand, under the Lorentz forcing of Case-P3, the flow is no longer separated and the streamline is attached to the entire surface of the cylinder. For Cases-O1, O2 and O3, the flow patterns are slightly changed although the flow is still oscillating, except for the forcing type of Case-O3 which shows a slight reduction of the oscillating amplitude. Similar flow patterns are found in

Figs. 10(h~j) under the Inward-normal LF where the flow exhibits an oscillating pattern. The Lorentz forcing of Case-I2 shows the reattached flow pattern with small reduction in the oscillating amplitude of the wake. It is interesting to find that the instantaneous flow patterns for Case-O2 and Case-I3 are similar to each other and the patterns for Case-O3 and Case-I2 are also similar to each other. The flow is greatly disturbed under the Negative Lorentz forcing of Cases-N1~N3. In the present computation, any distinct changes in flow pattern are not found under the Lorentz forcing of Inward-normal LF and Outward-normal LF applied in the entire cylinder circumference ($\theta=0\sim360°$) (Case-IF and Case-OF, respectively).

5. Conclusion

The present numerical results confirmed qualitatively the experimental results of Kim and Lee (2000) that the Positive Lorentz force has the effect of suppressing the flow separation, reducing the drag, and stabilizing the flow by making the symmetric flow pattern between the upper and lower sides of the circular cylinder.

In the condition of the present computation, it can be concluded that the effect of decreasing the drag force can be achieved by the Lorentz forcing types of (a) Outward-normal LF at $\theta=20°\sim80°$ from the fore stagnation point, (b) Inward-normal LF at $\theta=120°\sim180°$, (c) Positive LFs at $\theta=70°\sim130°$ and $\theta=120°\sim180°$, and (d) simultaneous forcing of the Outward-normal and Inward-normal LFs, respectively in the region of $\theta=20°\sim80°$ and $\theta=120°\sim180°((a)+(b))$. But it is found that the simultaneous forcing of (d) does not show the linearly superposed effect of the drag reductions of the independent two forcings, i.e. $\Delta C_D(a+b)<\Delta C_D(a)+\Delta C_D(b)$. It can be suggested that the effect of suppressing the oscillating lift force be achieved by inducing a symmetrical flow between the top and bottom regions of the circular cylinder. This effect can be obtained by the forcing modes of Positive LFs at $\theta=70°\sim130°$ and $\theta=120°\sim180°$.

It is expected that the results can provide useful information for efficient controlling of the flow around bluff bodies by using electromagnetic force.

References

Engelman, M. S. and Jamnia, M. -A., 1990, "Transient Flow Past a Circular Cylinder: A Benchmark Solution," *Int'l J. for Numerical Methods in Fluids*, Vol. 11, pp. 985~1000.

Hayase, T., Humphrey, J. A. C. and Greif, R., 1992, "A Consistently Formulated QUICK Scheme for Fast and Stable Convergence Using Finite-volume Iterative Calculation Procedures," *J. Comput. Phys.*, Vol. 98, pp. 108~118.

Henoch, C. W. and Meng, J. C. S., 1991, "Magnetohydrodynamic Turbulent Boundary Layer Control Using External Direct Current Crossed Surface Poles," *Annual Report IR/IED, Naval Underwater System Center*, TD 800.

Karniadakis, G. E. and Triantafyllou, G. S., 1989, "Frequency Selection And Asymptotic States in Laminar Wakes," *J. Fluid Mech.*, Vol. 199, pp. 441~469.

Kim, S. J. and Lee, Choung M., 1997, "Experimental Investigation of Flow Characteristics of a Magnetohydrodynamic (MHD) Duct of Fan-Shaped Cross-Section," *KSME J. (Korean Soc. of Mech. Eng.)*, Vol. 11, No. 5, pp. 295~302.

Kim, S. J. and Lee, Choung M., 2000, "Investigation of the Flow around a Circular Cylinder under the Influence of an Electromagnetic Field," *Experiments in Fluids*, Vol. 28, pp. 252~260.

Kim, S. J. and Lee, Choung M., 2001, "Control of Flows around a Circular Cylinder: Suppression of Oscillatory Lift Force," *Fluid Dynamics Research*, 29, pp. 47~63.

Meng, J. C. S., 1998, "Engineering Insight of Near-wall Microturbulence for Drag Reduction

and Derivation of a Design Map for Seawater Electromagnetic Turbulence Control," *Proc. of the International Symposium on Seawater Drag Reduction*, Newport, Rhode Island, USA, pp. 359 ~367.

Norberg, C., 1994, "An Experimental Investigation of the Flow around a Circular Cylinder: Influence of Aspect Ratio," *J. Fluid Mech.*, Vol. 258, pp. 287~316.

Nosenchuck, D. M. and D. Brown, 1993, "Discrete Spatial Control of Wall Shear Stress in a Turbulent Boundary Layer," *Proc. Near Wall Turbulent Flows*, Elsevier, pp. 689~698.

Persillon, H. and Braza, M., 1998, "Physical Analysis of the Transition'to Turbulence in the Wake of a Circular Cylinder by Three-dimensional Navier-Stokes Simulation," *J. Fluid Mech.*, Vol. 365, pp. 23~88.

Williamson, C. H. K., 1988, "Defining a Universal and Continuous Strouhal-Reynolds Number Relationship for the Laminar Vortex Shedding of a Circular Cylinder," *Phys. Fluids*, Vol. 31, pp. 2742~2744.